TU Delft

Delft University of Technology

Electrolyte effects on recirculating dense bubbly flow

An experimental study using X-ray imaging

Mandalahalli, Manas M.; Wagner, Evert C.; Portela, Luis M.; Mudde, Robert F.

DOI
10.1002/aic.16696

Publication date
2019

Document Version
Final published version

Published in
AIChE Journal

Citation (APA)
Mandalahalli, M. M., Wagner, E. C., Portela, L. M., & Mudde, R. F. (2019). Electrolyte effects on recirculating dense bubbly flow: An experimental study using X-ray imaging. *AIChE Journal*, *66*(1), Article e16696. https://doi.org/10.1002/aic.16696

Important note
To cite this publication, please use the final published version (if applicable).
Please check the document version above.

Copyright
Other than for strictly personal use, it is not permitted to download, forward or distribute the text or part of it, without the consent of the author(s) and/or copyright holder(s), unless the work is under an open content license such as Creative Commons.

Takedown policy
Please contact us and provide details if you believe this document breaches copyrights.
We will remove access to the work immediately and investigate your claim.

This work is downloaded from Delft University of Technology.
For technical reasons the number of authors shown on this cover page is limited to a maximum of 10.

Received: 7 February 2019 | Revised: 14 April 2019 | Accepted: 31 May 2019

DOI: 10.1002/aic.16696

TRANSPORT PHENOMENA AND FLUID MECHANICS

AIChE JOURNAL

Electrolyte effects on recirculating dense bubbly flow: An experimental study using X-ray imaging

Manas M. Mandalahalli | Evert C. Wagner | Luis M. Portela | Robert F. Mudde

Transport Phenomena Group, Department of Chemical Engineering, Delft University of Technology, Delft, The Netherlands

Correspondence
Manas M. Mandalahalli and Luis M. Portela, Transport Phenomena Group, Department of Chemical Engineering, Delft University of Technology, Van der Maasweg 9, Delft 2629HZ, the Netherlands.
Email: m.m.mandalahalli@tudelft.nl (M.M.M.) and l.portela@tudelft.nl (L.M.P.)

Funding information
NWO

Abstract

In this work, the effect of an electrolyte (up to 2 M of NaCl dissolved in water) on a homogeneous dense bubbly flow, in an airlift bubble column, is studied using non-intrusive techniques. X-ray and high-speed imaging are used to investigate the bubble size distribution, the local and the global gas-fraction profiles. The major effect of the electrolyte is the bubble size distribution at the fine-pore sparger, which is a consequence of the bubble coalescence inhibition promoted by the electrolyte. The bubble plume widening, the increase in overall gas fraction, and the onset of bubble recirculation in the column can all be explained by the bubble size reduction at the fine-pore spargers. As a result of the bubble size reduction, the overall role of the electrolyte is in a reduction of the driving force for the liquid recirculation. Furthermore, an accumulation of the small bubbles causes a layer of foam at the free surface, which is dynamic in nature and induces additional bubble recirculation.

KEYWORDS
bubble imaging velocimetry, bubble size, bubbly flow, coalescence inhibition, electrolytes, X-ray imaging

1 | INTRODUCTION

Electrolytes can be found in many industrial gas–liquid unit-operations, such as electrolysers, wastewater treatment, and froth flotations, for example.[1,2] In pneumatically agitated equipment, such as bubble columns, the bubble dynamics determines the mixing, heat, and mass transfer between the phases. Airlift or gaslift columns are a variant of the bubble columns, where the mixing also depends on the global circulation of the liquid; they have lower shear rates, shorter mixing times, and a larger operating-flow window, when compared with bubble columns; hence, they are widely used in chemical and bio-processes applications.[3]

The presence of surface active agents (such as electrolytes, dissolved organics, and surfactants in the liquid) can alter the performance of these processes. The complex hydrodynamics, combined with mass and heat transport, makes the design of airlift bubble columns still heavily reliant on phenomenological models. The majority of bubbly flow research has focused on ideal air–water systems and a better understanding of the effects of the surface active agents is needed, in order to develop efficient design models, in particular, for the airlift columns.

Several designs are used in airlift columns. The simplest design uses a configuration with an internal circulation, in which two sections, the riser and the downcomer, are divided by a draft tube or a separator plate (Figure 1a). The inter-relations between various flow and setup parameters (Figure 1b) determine the hydrodynamics of the bubbly flow.[4] The bubble size distribution (BSD) and the gas fraction are the parameters that determine the bubble residence time distribution and interfacial area, relevant for heat and mass transfer operations. The BSD and the heterogeneity of the flow are dependent on the selection of the sparger (type, material, and pore sizes), physical properties of the liquid, and the gas superficial velocity, v_{sg}.[5] Mudde

This is an open access article under the terms of the Creative Commons Attribution-NonCommercial License, which permits use, distribution and reproduction in any medium, provided the original work is properly cited and is not used for commercial purposes.
© 2019 The Authors. *AIChE Journal* published by Wiley Periodicals, Inc. on behalf of American Institute of Chemical Engineers.

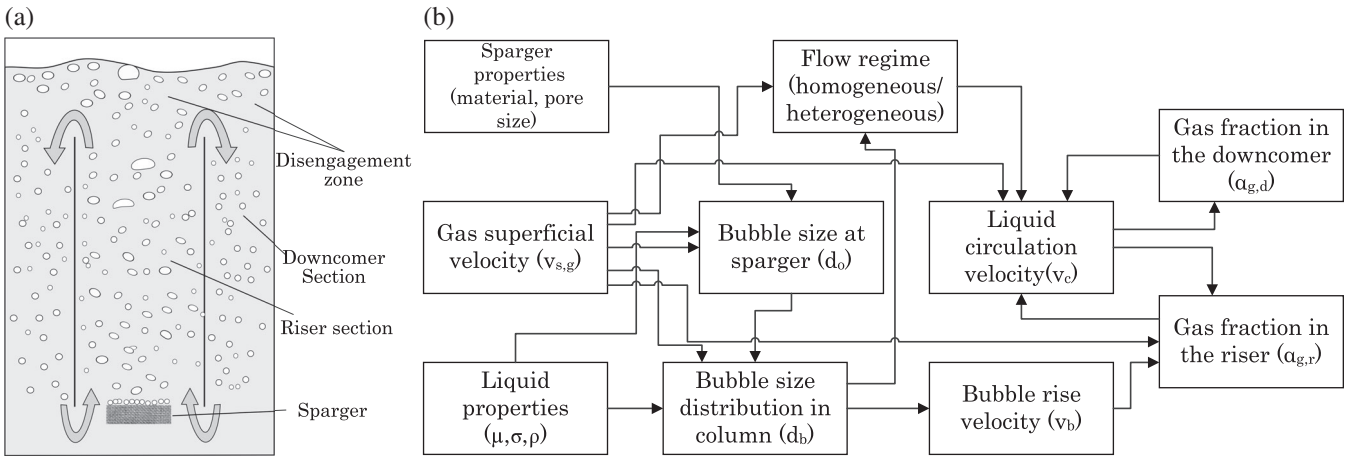

FIGURE 1 (a) Schematic of an internal airlift column. (b) Relationship diagram of variables in hydrodynamic design of an airlift column (inspired from HeijnenandRiet[4])

et al.[6] showed that an homogeneous bubbly flow can be achieved up to 55% gas fraction with an arrangement of fine-needle spargers. In particular, for airlift columns, the gas-fraction profile in the riser section determines the carryover of gas into the downcomer section.[7]

The role of electrolytes or inorganic salts can occur through three effects: (a) changes in the bulk liquid properties and a reported reduction in bubble rise velocity,[8] (b) a reduction in the bubble size at the sparger, and (c) impact on bubble–bubble interactions in the column and thereby on the BSD. Acting as "negative surfactants," the ions usually are repelled from the gas–liquid interface, inhibiting coalescence between bubbles.[9] The mechanism for coalescence inhibition can loosely be explained based on Marangoni effects, due to a slight increase in surface tension and the ion distribution at the interface.[10] For engineering purposes, the electrolyte effect is characterized by a transition salt concentration, C_{trans}, defined as the concentration beyond which the coalescence inhibition effect is observed between two bubbles.[11] For the salt considered in current study, sodium chloride (NaCl), the C_{trans} is found to be between 0.17 and 0.25 M (mol/L).[12] The bubble size reduction at the sparger, in presence of salt, is dependent on the pore density of the sparger, the salt concentration, and the gas superficial velocity. Reduced bubble sizes and thus increased residence time leads to an overall increase in the gas fraction.[13] Besides v_{sg}, bubble interactions in the column are dependent also on the local gas fraction. Besagni and Inzoli[14] observed formation of rapid moving noncoalescing "bubble clusters," even at low salt concentrations (0.17 M NaCl); this reduces the overall gas-phase residence time and the overall gas holdup. A better understanding of the electrolyte effect on bubble size and thereby on the gas fraction is therefore of interest in understanding the hydrodynamics of bubble columns and airlift columns.

The measurement of a polydispersed dense flow for spatial distribution of bubble sizes and gas fraction is a challenge. Noninvasive high-speed imaging and further image processing can provide a detailed picture of the BSD, bubble velocities, and local gas fraction.[15] However, at large gas fractions in a wide column, the acquisition is limited to near-wall regions, making the extrapolation to the entire column unreliable. Optical probes can provide single point measurements for bubbles substantially bigger than the tip size; however, the use of multiple probes can potentially disrupt the flow.[16] As optical probes can only detect bubbles larger than the tip size, with a large fraction of small bubbles at high salt concentrations, this would lead to a bias toward a smaller fraction of bigger bubbles determining the local gas fraction. Radiation-based techniques such as X-ray imaging have been widely used to characterize dense multiphase flows: fluidized bed,[17] slurry bubble columns,[18] and granular flows.[19] The X-ray imaging technique usually has a good spatial resolution, however, at a laboratory scale is limited by time averaging.[20] This limitation can be overcome by using high-speed X-ray radiography. However, high-speed X-ray radiography usually requires specialized equipment and large synchrotron X-ray source.[21]

The aim of this work is to get a better understanding of the effect of dissolved salt, over a large concentration range (0–2 M NaCl), on a homogeneous bubbly flow, in an airlift column. The role of salt, in the bubble plume behavior and the gas carryover in to downcomer section, is understood through its impact on the BSD at fine-pore bubble spargers. The use of high-speed imaging and X-ray imaging techniques, for measurement of the BSD, the time-averaged local and global gas fractions are explained in-detail in the next section. To further explain the airlift column hydrodynamics, in electrolyte solutions, as a consequence of the bubble size reduction, a comparison of the experimental results is made with a simple one-dimensional (1D) drift-flux liquid recirculation model, based on the measured average bubble size at the fine-pore sparger. The model is further explained in Section 7.

2 | EXPERIMENTAL METHODOLOGY

2.1 | Experimental setup and X-ray imaging

Experiments are performed in an internal loop airlift bubble column ($W \times D \times H$ = 300 mm × 100 mm × 1,000 mm), with riser section

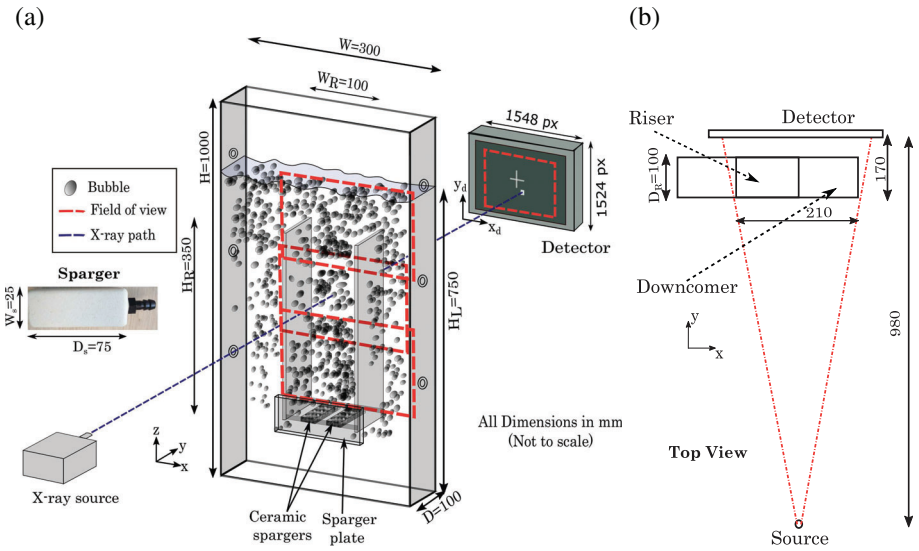

FIGURE 2 Airlift column setup: (a) schematic with column and sparger dimensions, rectangles showing the overlapping X-ray fields of view; (b) top view showing the location of the column with respect to the X-ray source detector [Color figure can be viewed at wileyonlinelibrary.com]

dimensions equal to $W_R \times D_R \times H_R$ = 100 mm × 100 mm × 400 mm. In order to avoid additional X-ray attenuation and salt-induced corrosion, metal components are not used; the setup is built using perspex, with fittings made of perfluoroalkoxy alkanes (PFA) polymer. The column, as shown in Figure 2, is equipped with two ceramic fine-pore bubble spargers (Pentaires), with an average pore size of 50 μm and dimensions, $W_s \times D_s \times H_s$ = 25 mm × 75 mm × 25 mm, placed at the bottom of the riser section (200 mm above the bottom of the column). The spargers are attached to the front end of the column using a sparger plate that extends 50 mm into the riser section. The bottom surface of the spargers is sealed with glue, to avoid accumulation of gas bubbles. The degassed liquid height is maintained at H_L = 750 mm (150 mm above the riser section). Demineralized water and nitrogen gas are used as the liquid and gas phases, respectively. Purified sodium chloride (laboratory grade NaCl) is used as salt, at concentrations: 0.2, 0.5, 1, and 2 M. The gas flow rate is controlled by a thermal mass flow controller (Bronkhorst B.V.). Change in fluid properties (density, viscosity, and surface tension), due to electrolyte addition, are shown in Table 1. The superficial gas velocity, v_{sg}, defined as the ratio of the inlet gas flow rate to the riser cross-sectional area, is varied in the range of 0.8–4.8 cm/s.

A source-detector pair is used to measure the attenuation of the X-ray through various sections of the airlift column. In order to include both the riser and downcomer sections in the field of view, the column is placed close to the detector, as shown in the top view, Figure 2b. The X-ray measurements are performed in three overlapping field-of-views, above the sparger plate (shown in rectangles in Figure 2a). The source is operated at 120 KeV and 1.6 mA, in order to achieve maximum contrast between the water and gas phases. The spot size of the X-ray source is 1 mm. The flat detector (Xineous-3131 CMOS model), consists of a 307 mm × 302 mm X-ray sensitive area, with a 1,548 × 1,524 pixel array. Each pixel has a size of 198 μm × 198 μm, with 14 bits of pixel depth, with maximum intensity counts equal to 16,000. The image acquisition frequency is 20 Hz.

TABLE 1 Electrolyte effect on physical properties of water at 20 ° C[22]

Salt concentration	Density	Viscosity	Surface tension
C_s (M NaCl)	ρ (kg/m^3)	μ (Pa s, ×10^{-3})	σ (mN/m)
0 (water)	999	1.002	72.2
0.2	1,010	1.04	72.8
0.5	1,022	1.06	73.4
1.0	1,042	1.104	74.8
2.0	1,085	1.22	76.4

The measurement principle of X-ray imaging is based on the Beer–Lambert law. The intensity of each pixel on the detector, I_{pixel}, is a function of the thickness, X, and the attenuation coefficient, μ_0, of the material placed between the source and the pixel. The intensity attenuation is given by:

$$\frac{I_{pixel}}{I_0} = \exp(-\mu_0(E)X). \quad (1)$$

The μ_0 is dependent on the energy distribution of the X-ray source. I_0 is the intensity on the pixel without the presence of the material between the source and the detector. The polychromatic nature of the X-ray source leads to preferential absorption of low-energy radiation, known as *beam hardening*, for example.[23] The close packing of detector pixels compared with the distance between source and detector can cause scattering effects. In current work, for practical purposes, the nonlinear aspects of attenuation (beam hardening and scattering) are lumped into a constant, C, leading to a two-parameter version of the Beer–Lambert equation:

$$\log(I_{pixel}) = -\mu X + C, \quad (2)$$

where, $\mu = \mu_0 l_0$. Considering the density difference between the gas and liquid phases, absorption of the X-ray is associated with the pathlength of water phase between the source and each pixel of the

detector. Thus, the pixel-wise gas fraction, averaged along the X-ray path, can be obtained by measuring the intensities with and without the gas bubbles, I_{gas} and I_{nogas}, respectively,

$$\alpha_{g,pixel} = \left(\frac{X_{nogas} - X_{gas}}{X_{nogas}}\right) = \frac{1}{(\mu \times X_{nogas})} \cdot \log\left(\frac{I_{gas}}{I_{nogas}}\right). \quad (3)$$

2.2 | Calibration and validation

Besides the two-dimensional (2D) coordinate (x_d, y_d) on the detector and the pathlength through water, the no-gas pixel-wise intensity (I_{nogas}) is also dependent on the dissolved electrolytes. Both sodium and chloride ions have valence electrons, leading to a higher attenuation of the radiation than in pure water. The difference between the attenuation in water with dissolved salt and the pure water is proportional to the salt concentration, C_s.

The X-ray coefficients (μ and C) for each pixel on the detector are obtained using a four-point calibration method. Four rectangular columns with depths 60, 90, 120, and 150 mm, filled with water, are used to record I_{pixel}. The resultant 2D intensity resembles a cone-beam profile, which is a characteristic of the diverging X-rays from the source. A line intensity profile on the dectector, therefore, is parabolic in nature (Figure 4b). The cone-beam profile is fitted by a second-order polynomial in each direction of the detector, as shown in Figure 3a. This curve is obtained for different salt concentrations and column depths. Pixel-wise data are further fitted to the simplified Beer–Lambert equation (Equation (2)). The resultant curve generated is in good agreement with the raw experimental data, as seen for a random pixel in Figure 3b.

The reliability of the four-point calibration method to compute the steady-state gas fraction is tested using a phantom method. Three straws, made of polystyrene with internal diameters of 2.8, 5.3, and

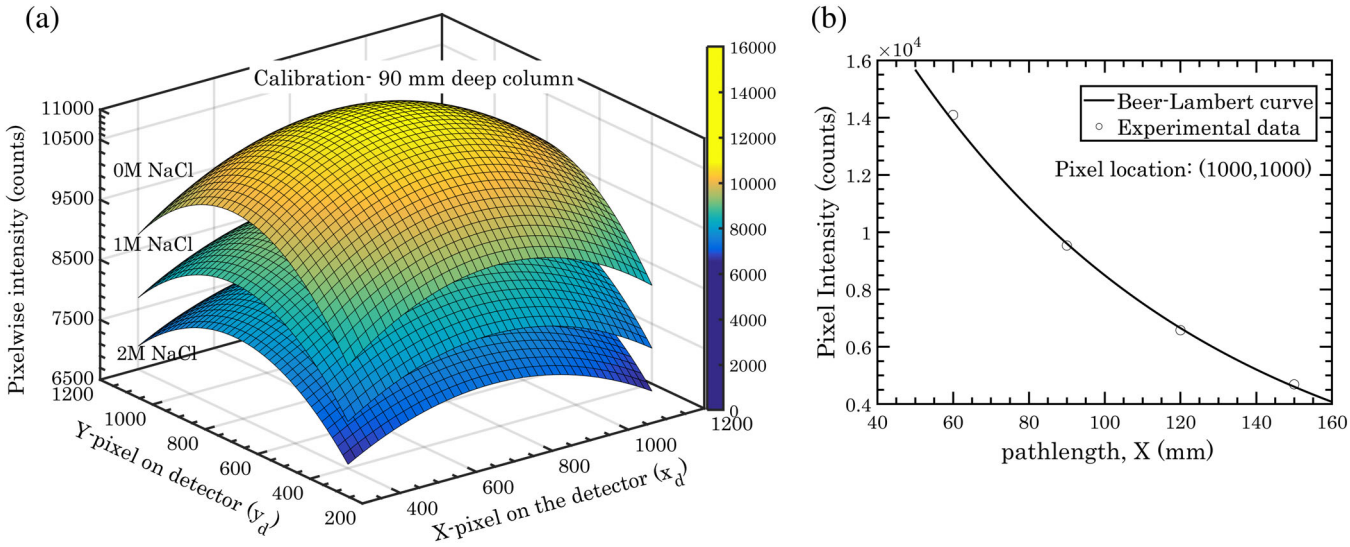

FIGURE 3 Pixel-wise calibration of intensity: (a) cone-beam calibration profile for 90-mm deep column for different salt concentrations; (b) comparison of interpolated Beer–Lambert curve with experimental data on a random pixel (x, y) = (1,000, 1,000) on the detector [Color figure can be viewed at wileyonlinelibrary.com]

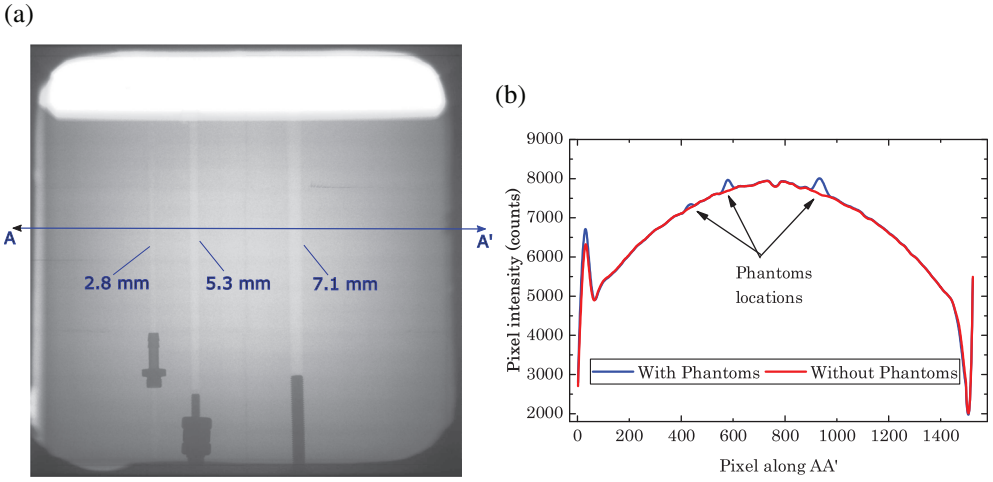

FIGURE 4 Phantom validation of gas-fraction calibration: (a) contrast image on the detector; (b) horizontal line intensity profile along line AA′ with and without phantom [Color figure can be viewed at wileyonlinelibrary.com]

7.1 mm, are placed in the 120 mm deep column, corresponding to 2.3, 4.4, and 5.9% void fraction, respectively. Absorption due to the wall material of the phantoms is ignored due as the attenuation coefficient of polystyrene at 120 KeV ($\mu_{poly.st}$ = 1.49) is similar to that of water (μ_{water} = 1.505). The contrast-enhanced X-ray image and resultant intensity variation are shown in Figure 4. The maximum deviation of the experimental value from the theoretical gas fraction, obtained from the phantom diameters, is found to be 0.45% (4.5 x 10^{-3}) in absolute value.

2.3 | Local and overall gas-fraction evaluation

The current X-ray system, in spite of its good pixel-wise spatial resolution, has a limited temporal resolution, with an acquisition rate of 20 Hz; at this low acquisition rate, the pixel-wise gas fraction will contain an error induced by the blurring motion of the bubbles. As the pixel size (0.2 mm) is much smaller than the typical bubble sizes (3 mm), averaging of the pixel-wise data is required, both spatially and temporally. Pixel binning is done by considering a rising 3 mm bubble with typical velocity of 0.3 m/s. In 1/20 s, the bubble would create a vertical blur of 15 mm. In a dense bubbly flow, the flow is predominant in the vertical direction ($v_y >> v_x$); the bubble wiggle distance is taken as 1.5 times typical bubble diameter, that is, 4 mm. This is done in order to obtain enough data points for a lateral gas-fraction profile. To calculate the local gas fraction, the pixel-wise gas-fraction data are spatially averaged over a window size of 15 mm ×4 mm. Furthermore, the data are cumulatively averaged over 15 s, to reduce the fluctuations to less than 5% of the value.

In order to determine the overall gas fraction, the top surface is tracked using X-ray imaging. Note that this height does not include the foam layer at the top, as the amount of liquid in the foam is beyond the sensitivity of the X-ray measurements. As can be seen in Figures 6 and 15, the thickness of this foam layer is few millimeters. Hence, its exclusion introduces an error in the overall gas fraction smaller than 0.4% (4 x 10^{-3}) in absolute value.

2.4 | High-speed imaging: Bubble size measurement and bubble image velocimetry

Quantitative visualization is performed using a high-speed camera (PCO.dimax s4, 2016 pixel × 2016 pixel resolution at 1,000 fps) to obtain the BSD and the bubble velocity.

2.4.1 | Bubble size

In order to characterize the sparger, images of the bubbles, rising from an individual sparger are captured, 10 mm above the sparger surface. The field of view is 17 mm × 17 mm (118.6 pixel/mm resolution), focused at the mid-sparger depth. With a shallow focal depth (few mm, with an aperture f/1.8), in-plane bubbles are separated from the bubbles in the background. Overlapping bubbles from close-by planes are segmented using a distance transform watershed method. The images are analyzed using an open-source image processing software FIJI, to obtain the BSD. The purpose of this measurement is two-fold: (a) to understand the influence of salt addition on the BSD in the plume originating from each sparger and (b) to provide the average bubble size as an input for a simple 1D mechanistic model (described in Section 7).

2.4.2 | Bubble velocity

Bubble image velocimetry (BIV) technique is used to compute the bubble velocity in the disengagement zone. In BIV, similar to traditional particle image velocimetry (PIV) technique, a correlation between successive images is used to determine the bubble velocity. However, unlike the traditional PIV technique, BIV does not require a laser illumination.[24] The images are acquired at 1,000 fps in the disengagement zone with a field of view of 20 cm × 20 cm. Using a shallow focal depth (with aperture f/1.8), the *texture* of the gas–liquid interface can be captured with shadowgraphy imaging, similar to a sheet illumination. Subsequently, the images are inverted and cross correlated using standard PIV algorithms in LaVision DaVis 8.0 software.

3 | SALT EFFECT ON BUBBLES FORMED AT THE SPARGER

Bubble growth is dependent on the sparger type (material, pore size, and spacing).[5] The airstone-type spargers used in the current study have smaller and closely packed pores, in comparison with other spargers, typically used in bubbly flow investigations (needle, ring-type, and spyder-type). As bubble size in the column is dependent on the bubble size during growth, it is essential to determine the BSD at the sparger.

Bubble sizes are measured from bubble images, acquired 10 mm above the surface of an individual sparger. Images captured along the width of the sparger, give an indication of the size distribution and width of the rising plume. In the water case, the BSD is unimodal with a peak diameter around 2.3 mm (Figure 5a). In the salt case, however, the distribution changes to bimodal with increasing C_s, with a large fraction of micron size bubbles. This is due to the inhibition of coalescence between the bubbles during the growth stage.[13] These smaller bubbles cluster toward the core of the bubble plume. Figure 5b shows the modes of the BSD along the bubble plume. Bubbles rising along the side surface of the sparger have longer contact times, leading to a higher probability of coalescence; therefore, larger bubbles are observed toward the edges of the plume. An increase in flow rate or addition of salt increases the overall number of bubbles, thereby increasing the net bubble–bubble interactions. A direct impact is observed by the measurement of the bubble plume width, as shown in Figure 5c.

With the current spargers, the interaction of bubbles is much higher than in a large pore spyder-type sparger, used in the recent work of Besagni and Inzoli.[14] Consequently, the effect of the salt-induced coalescence inhibition on the BSD close to the sparger is much larger, in comparison to their work.

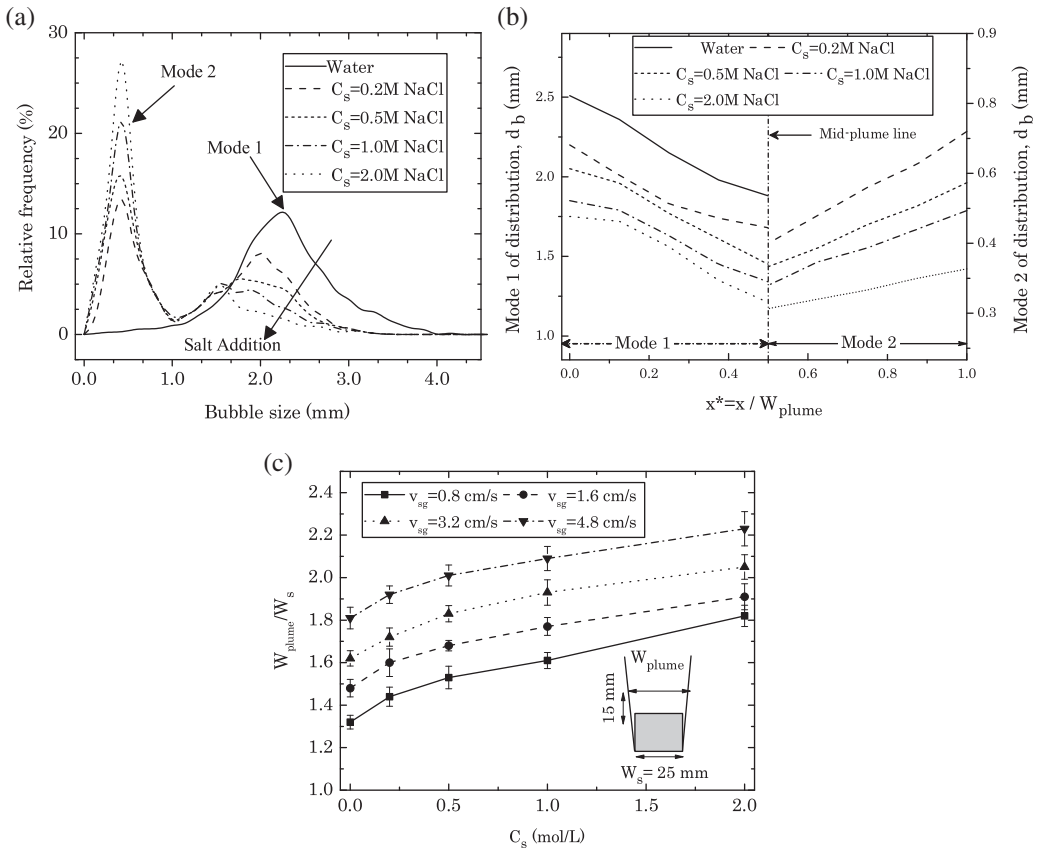

FIGURE 5 (a) Bubble size distribution in the plume above an individual sparger (measured 1 cm above the surface), v_{sg} = 1.6 cm/s. (b) Variation of modes of bubble size distribution as a function of lateral coordinate in the plume, v_{sg} = 1.6 cm/s (corresponding Modes 1 and 2 of the distribution are depicted in Figure 5a). (c) Nondimensional plume width for different v_{sg}. Note that these single sparger measurements are performed at half the inlet gas flow rates used in airlift bubble column experiments. The superficial velocities, v_{sg} is calculated based on the cross-sectional area of the riser section (100 mm × 100 mm)

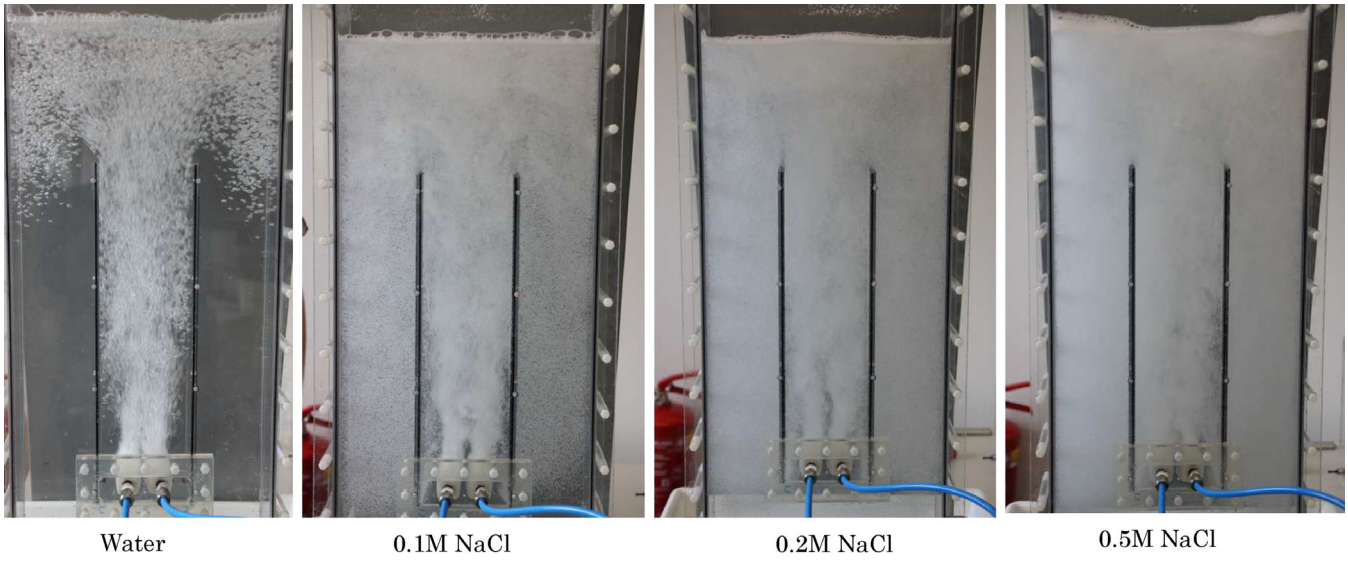

FIGURE 6 Salt effect on the flow pattern, at v_{sg} = 1.6 cm/s [Color figure can be viewed at wileyonlinelibrary.com]

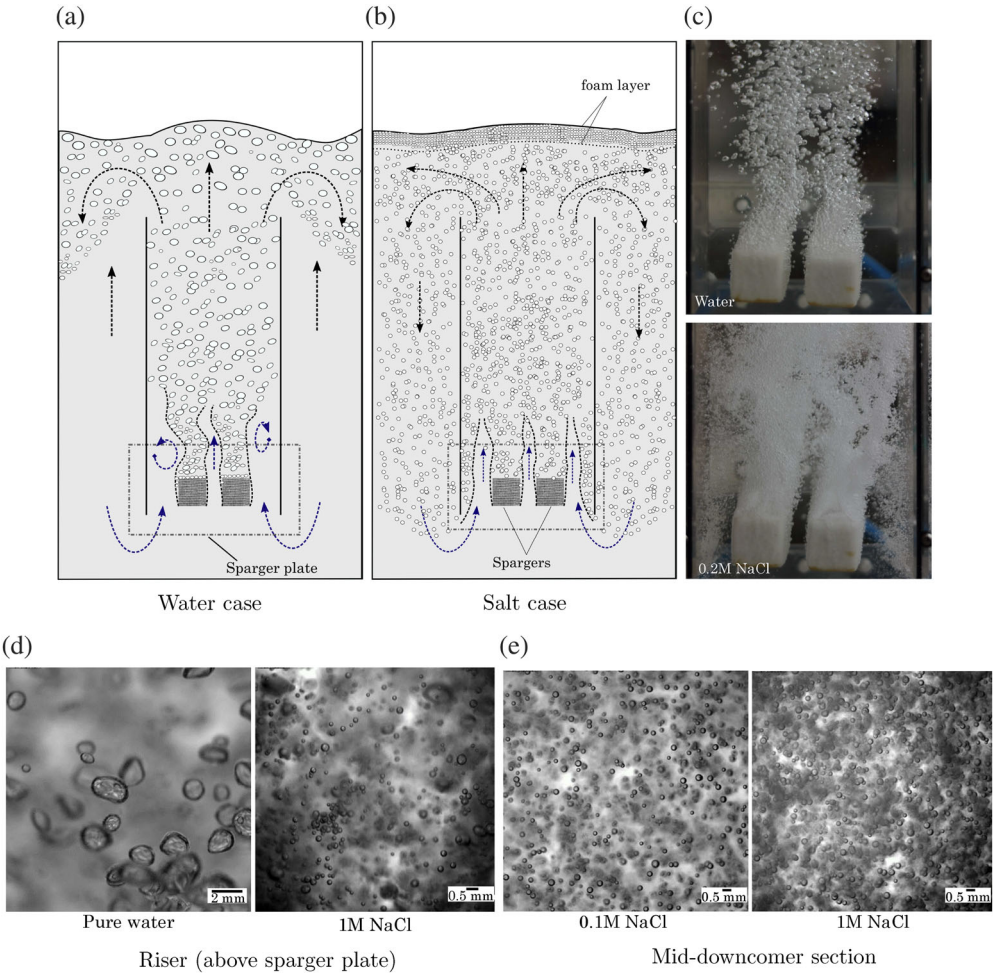

FIGURE 7 Schematic of flow patterns: (a) water case; (b) salt case; (c) snapshots of the sparger region at v_{sg} = 1.6 cm/s, top: water, bottom: 0.2 M NaCl; (d, e) high-speed images of the bubbles at v_{sg} = 1.6 cm/s (field of view: 17 mm × 17 mm): (d) riser section (above the sparger plate) and (e) mid-downcomer section [Color figure can be viewed at wileyonlinelibrary.com]

4 | FLOW PATTERNS

Figure 6 shows the effect of salt addition on flow patterns in the airlift column. In the water case, no or little bubble recirculation is observed. High-speed images above the sparger plate qualitatively show the results obtained in Figure 5a. Bubble of sizes in the range 2–3 mm are measured (Figure 7d, left). Due to a typical low slow slip, the bubbles are dragged into the top part of the downcomer section (below the airlift separator) along with the recirculating liquid, only to be balanced by the counteracting buoyancy force, as illustrated in Figure 7a. The resulting recirculation creates a oscillatory behavior between the riser section and the two legs of the downcomer sections. Liquid recirculation affects the bubble plume rising from the sparger, meandering the plume closer to the center of the riser section (Figure 7c, top). With increasing gas superficial velocity, an increased gas carryover to the downcomer section is observed, which can be attributed to an increase in liquid circulation velocity.

With increasing NaCl concentration (C_s), Figure 6 shows an increase in bubble recirculation, leading to a higher degree of opaqueness of the flow. Owing to the salt-induced coalescence suppression at the sparger, bubbles as small as 150–200 μm are observed (Figure 7d, right). Due to the lack of sufficient buoyancy force, these bubbles recirculate into the downcomer section. With an increasing C_s, a fractional increase in small bubbles at the sparger (Figure 5a) leads to a net increase in the fraction of smaller bubbles recirculating into the downcomer section (Figure 7e). Similarly with higher v_{sg}, micron size bubbles are predominant, due to a lower contact time between the bubbles during growth. The recirculating bubbles rise along the walls of the riser section (Figure 7c, bottom) and interact with the bubble plumes above the sparger plate.

Other effect of salt addition is the formation of a finite layer of foam (typical a few mm in thickness) at the top liquid free surface. This is a result of accumulation of micron size bubbles, from coalescence inhibition at the spargers. These bubbles do not disengage from the column, as the salt concentration in the inter-foam liquid prevents it from coalescing with the continuum gas.[25] Consequently, as seen in Figure 6, the thickness of the foam layer increases with increasing salt concentration, C_s. Oscillation of the free surface, with and without the foam layer is relevant for the dynamics of the disengagement zone. This is discussed further in Section 8.

5 | LOCAL GAS FRACTION IN THE RISER SECTION

The profile of the time-averaged local gas fraction above the sparger plate shows an expected M-shape profile (Figure 8a). The peaks

correspond to the gas fraction at the centers of the fine-pore spargers. With increasing superficial velocity (v_{sg}), there is an increase in overall number of bubbles, and thus an increased gas fraction. However, the lateral profiles are similar in structure.

At a constant flow, with addition of salt, the bubble plume widens (Figure 8b). This is a result of the interaction of the bubble plumes with the recirculating bubbles. Besides this, the liquid velocity between the plume and the wall is lower than the velocity in the sparger gap, due to the dispersed bubbles. The resulting difference in entrainment leads to an asymmetry and the core of the plume moving toward the wall. Similar observations were made by Freire et al.,[26] studying plume–plume and plume–wall interactions.

The lateral gas-fraction profile along the riser section for two superficial velocities (v_{sg}=0.8 and 3.2 cm/s) are shown in Figure 9. With an increase in v_{sg}, the profiles are structurally similar, with few differences. At a higher superficial velocity, there is larger fraction of recirculating bubbles, which is consistent with visual observation. At higher gas flow, with larger number of bubbles, there is a net higher buoyancy force in the plume. This results in a higher degree of meandering of the plume. Width of the individual plume also increases, due to a strong bubble dispersion in the longitudinal direction. Consequently, the plume merging is slightly faster (or at an earlier height) than at a lower flow rate. Beyond 25% of riser height ($h = H_R/4$), flattening of the radial gas-fraction profile is observed. At the riser top, the flow reaches a homogeneous radial profile. There is a clear distinction between the water and the salt case, whereas the actual concentration of the salt has little effect on the local gas fraction.

6 | OVERALL GAS FRACTION AND EFFECT OF INITIAL LIQUID HEIGHT

The overall gas fraction, measured by an increase in the liquid height, due to gas sparging, is shown in Figure 10. The linear dependence of

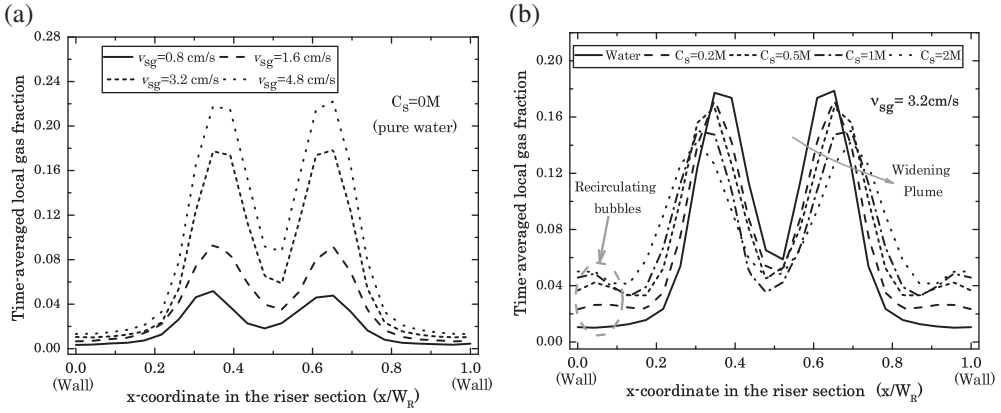

FIGURE 8 Gas-fraction profile in riser section (measured above the sparger plate, 250 mm from the bottom of the column): (a) effect of gas flow rate without salt and (b) effect of salt addition with gas superficial velocity, v_{sg} = 3.2 cm/s. Same measurement locations have been used to compare pure water and salt cases

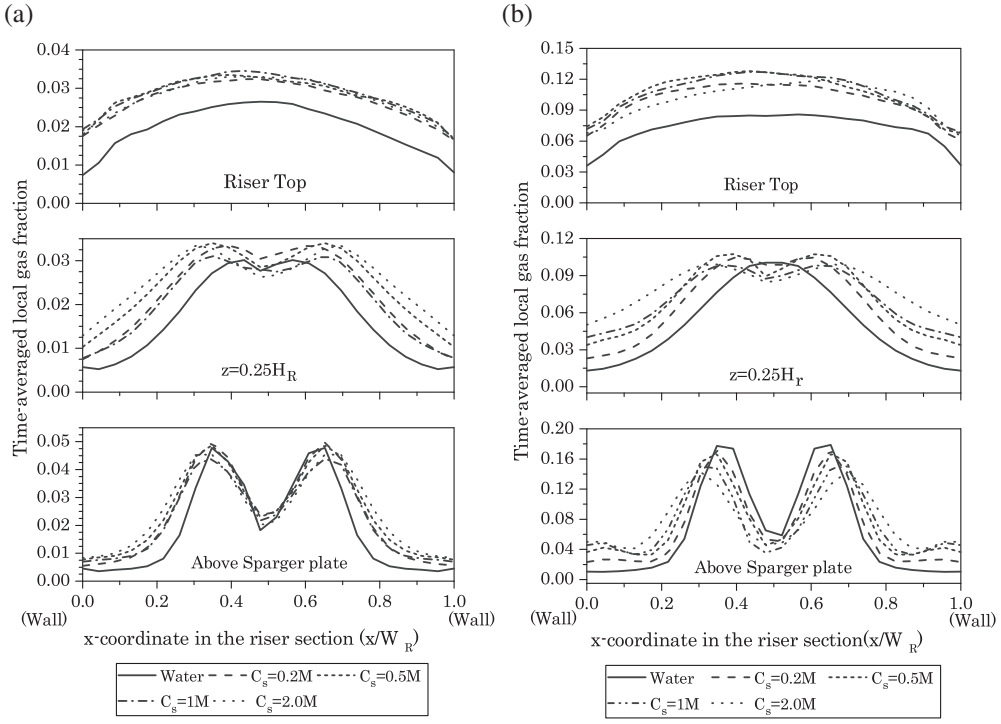

FIGURE 9 Gas fraction in the riser section for (a) v_{sg} = 0.8 cm/s and (b) v_{sg} = 3.2 cm/s. Measurement locations: distance from bottom of the column (z), above sparger plate: z = 250 mm; $H_R/4$: z = 340 mm; riser top: 580 mm

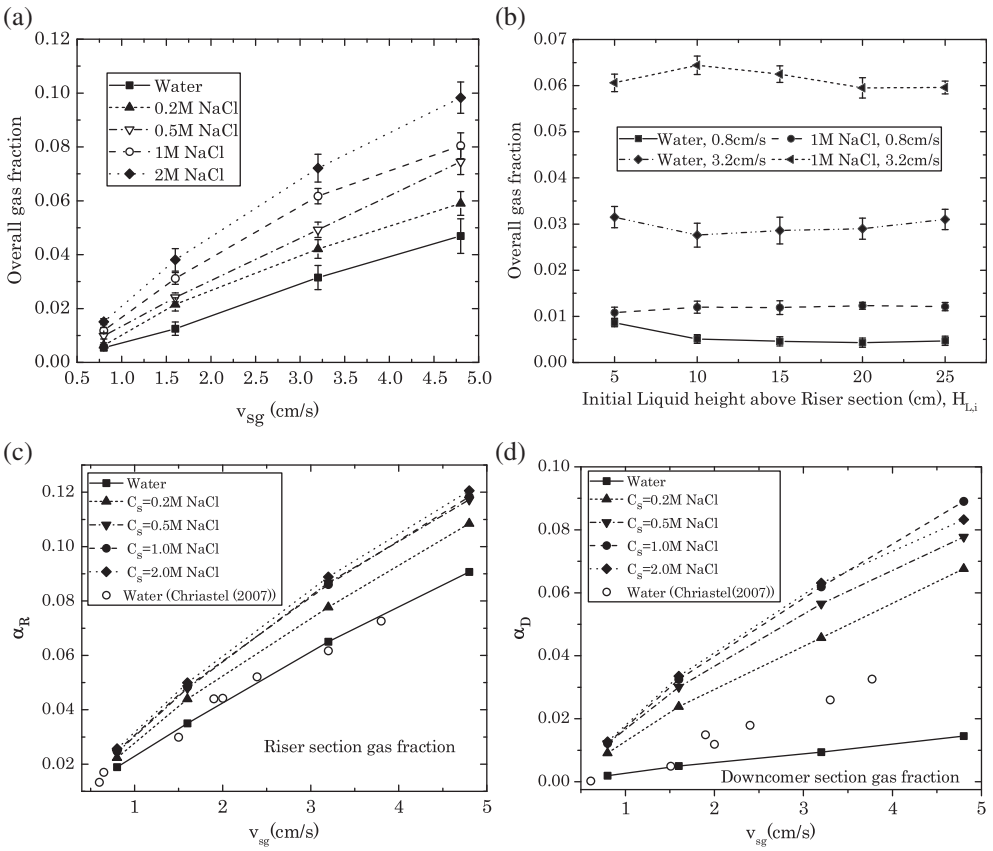

FIGURE 10 Overall gas fraction as a function of: (a) superficial gas velocity, v_{sg}, for initial height $H_{L,i}$ = 15 cm and (b) initial liquid height, $H_{L,i}$. (c, d) Section-wise averaged gas fraction: (c) riser section (data for salt concentrations, C_s = 0.5 M,1.0 M and 2.0 M are close to each other) and (d) downcomer section. Lines are for visual purposes and do not indicate a trend

gas fraction with the superficial velocity is a characteristic of a flow in homogeneous regime. Previous studies on airlift columns with a sea water salt concentrations (0.15 M) show an increase in overall gas fraction.[27] Studies in bubble columns, with a wide range of electrolyte concentrations,[28-30] observed no effect or even a slight decrease in the gas fraction, beyond the transition concentration ($C_{trans} \approx$ 0.17 M), owing to the formation of bubble clusters with rise velocities larger than individual small bubbles. In the current study, however, no bubble clusters are observed. An increase in gas fraction beyond C_{trans} can be attributed to enhanced recirculation of gas bubbles (Figure 6) and thus increased residence times for smaller bubbles. Section-wise gas fraction, for the riser and the downcomer sections (Figures 10c, d)), show a marginal change at higher salt concentrations.

The initial liquid height is an important parameter in design of airlift columns. Experiments performed with five different initial liquid heights ($H_{L,i}$) shows a noneffect on the overall holdup, within experimental error (Figure 10b). This is the case for both water and electrolyte situations, at different superficial gas velocities. Slight difference at $H_{L,i}$ = 5 cm (liquid height above the riser section) is due to squeezing effect on the recirculating two phase flow caused by the close proximity of the free surface to the separator plate.

7 | MECHANISTIC MODEL FOR BUBBLE SIZE EFFECTS

In previous sections, electrolyte effects on the local and global gas fractions have been explained as a consequence of its impact on the BSD at the fine-pore spargers. We use a simple 1D-mechanistic model, based on the drift-flux method,[31] to understand the effect of bubble size on the hydrodynamics of the airlift column. The goal is to see whether the variation of the bubble size at the sparger can explain the experimental observations.

7.1 | Drift-flux model for airlift columns

Drift-flux model is used to solve two-phase flows in pipes, bubble columns, airlift columns, and so forth, considering the mixture as a whole, rather than two separate phases. The model is based on the existence of a slip velocity between the two phases, as a condition for surface motion. The superficial velocities of the dispersed gas phase (j_d) and the continuous liquid phase (j_c) are related to the gas fraction by a correlation from the work of Richardson and Zaki,[32] as:

$$(1-\alpha)\frac{j_d}{v_\infty} - \alpha\frac{j_c}{v_\infty} = \alpha(1-\alpha)^n, \quad (4)$$

where, v_∞ is the terminal velocity of a single rising bubble in an infinite medium and the exponent, n, is a function of the Reynolds number (Re) as 4.45 $Re^{-0.1}$ for $1 \le Re \le 500$ and 2.39 for $Re \ge 500$. v_∞ as a function of the bubble size can be obtained from the emperical curve, proposed by Clift et al.[33] (p. 172). For the salt cases, data from the contaminated water curve are used. For the riser and the downcomer sections, separate versions of Equation (4) are set up, as the gas fractions in both sections will be different.

A schematic of two-phase flow in the airlift column is set up as shown in Figure 11a. The drift-flux model is based on a steady-state mechanical energy balance between the gravity forces and the frictional forces. Driving force for recirculation is the density differences between the riser and the downcomer sections (Zones 2 and 4 in Figure 11a, respectively). The frictional effects are due to wall friction and flow reversals at the top disengagement section (Zone 3) and bottom (Zone 5). The mechanical energy balance, between the riser and each half of the downcomer sections, is defined as:

$$\underbrace{H_L \cdot g \rho_L (\alpha_R - \alpha_{D,i})}_{\text{Driving force for recirculation}} = \underbrace{\lambda_{f,R} \frac{H \rho_{m,R}}{d_R} j_{c,R}^2 + \lambda_{f,D,i} \frac{H \rho_{m,R}}{d_{D,i}} j_{c,D,i}^2}_{\text{Pressure drop due to longitudinal flow}} + \underbrace{K_{w,R} \rho_L j_{c,R}^2 + K_{w,D,i} \rho_L j_{c,D,i}^2}_{\text{Pressure drop due to 90° bends}}, \quad (5)$$

where i = 1,2 denotes each half of the downcomer sections. Detailed derivation of Equation (5) and correlations for the friction factors ($\lambda_{f,R}$, $\lambda_{f,D,i}$, $K_{w,R}$, and $K_{w,D,i}$) are available from the work of Chriastel et al.[34]

$$\lambda_{f,R} = 0.21 \frac{\sqrt{g d_R}}{j_{c,R}} \sqrt{\alpha_R}; \quad \lambda_{f,D,i} = 0.28 \frac{\sqrt{g d_b}}{j_{c,D,i}} \sqrt{j_{c,D,i}}; \quad K_{w,R} = \frac{1}{(1-\alpha_R)^2}; \quad K_{w,D,i} = 2, \quad (6)$$

where $d_b = d_{b,avg} = f(C_s)$ is the average bubble diameter, obtained from the BSD measurements. The liquid circulation velocity, v_c, is obtained by a simple mass balance for the liquid phase.

$$2 v_c H = d_R j_{c,R}. \quad (7)$$

Similarly, the gas superficial velocities are coupled as:

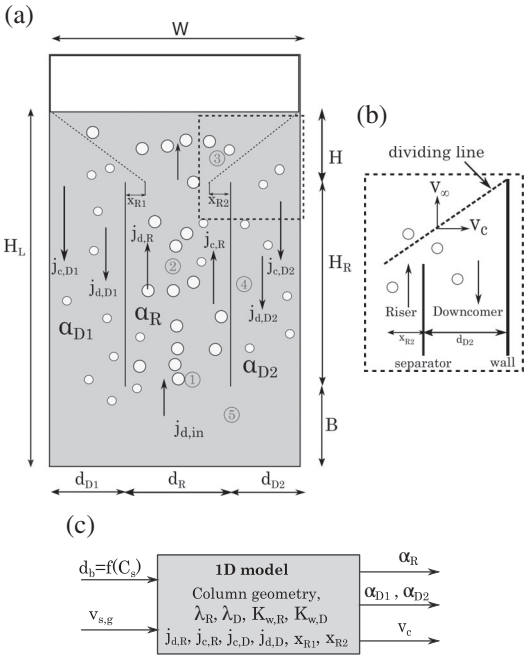

FIGURE 11 (a) Schematic of the drift flux model with different zones marked: 1, sparger section; 2, riser (above sparger plate); 3, disengagement zone; 4, downcomer section; 5, bottom gas recirculation. (b) Modeling of gas carryover into downcomer section. (c) Variables involved in the one-dimensional model

$$A_R j_{d,R} = A_R j_{d,in} + A_{D1} j_{d,D1} + A_{D2} j_{d,D2}, \quad (8)$$

where A_R, A_{D1}, and A_{D2} are, respectively, the cross-sectional areas of the riser and two legs of the downcomer section. $j_{d,in} = v_{sg}$ is the inlet gas superficial velocity.

7.2 | Model for gas recirculation and results from 1D model

A standard implementation of the model, as described above, does not consider the effect of gas recirculation on the increased riser section gas fraction; hence, it requires an additional experimental input via measurement of the liquid superficial velocity in the downcomer section (usually measured with salt-tracer techniques[34]). In order to better explain the bubble size effect on recirculation, instead of the additional measurements, we consider a model for the gas carryover into the downcomer section, as shown in Figure 11b. Here, $x_{R,i}$ (i = 1,2) is defined as the regions close to the wall of the riser section, where the flowing bubbles are dragged into the corresponding downcomer section. At the top disengagement section (Zone 3), a zero horizontal slip velocity is assumed. This way, bubble rising out of a section of the column (defined by the dividing line), manage to escape toward free surface, whereas the trajectories below the dividing line flow into the downcomer section.

The gas-phase superficial velocity in the downcomers can be estimated from:

$$j_{d,D,i} = \frac{x_{R,i}}{d_R} j_{d,R} \quad \text{if} \quad x_{R,i} \le 0 \rightarrow j_{d,D,i} = 0$$
$$\frac{x_{R,i} + d_{D,i}}{H} = \frac{v_c}{v_\infty} \quad (9)$$

It is noted here that the circulation velocity v_c is defined as the actual velocity and not the superficial velocity.

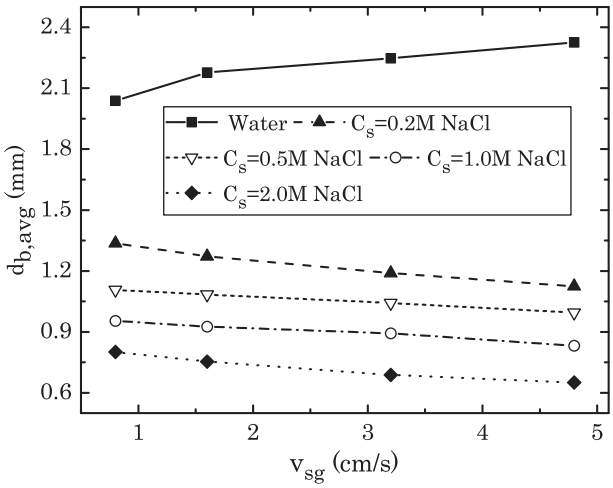

FIGURE 12 Average bubble size, $d_{b,avg}$, measured from a single sparger

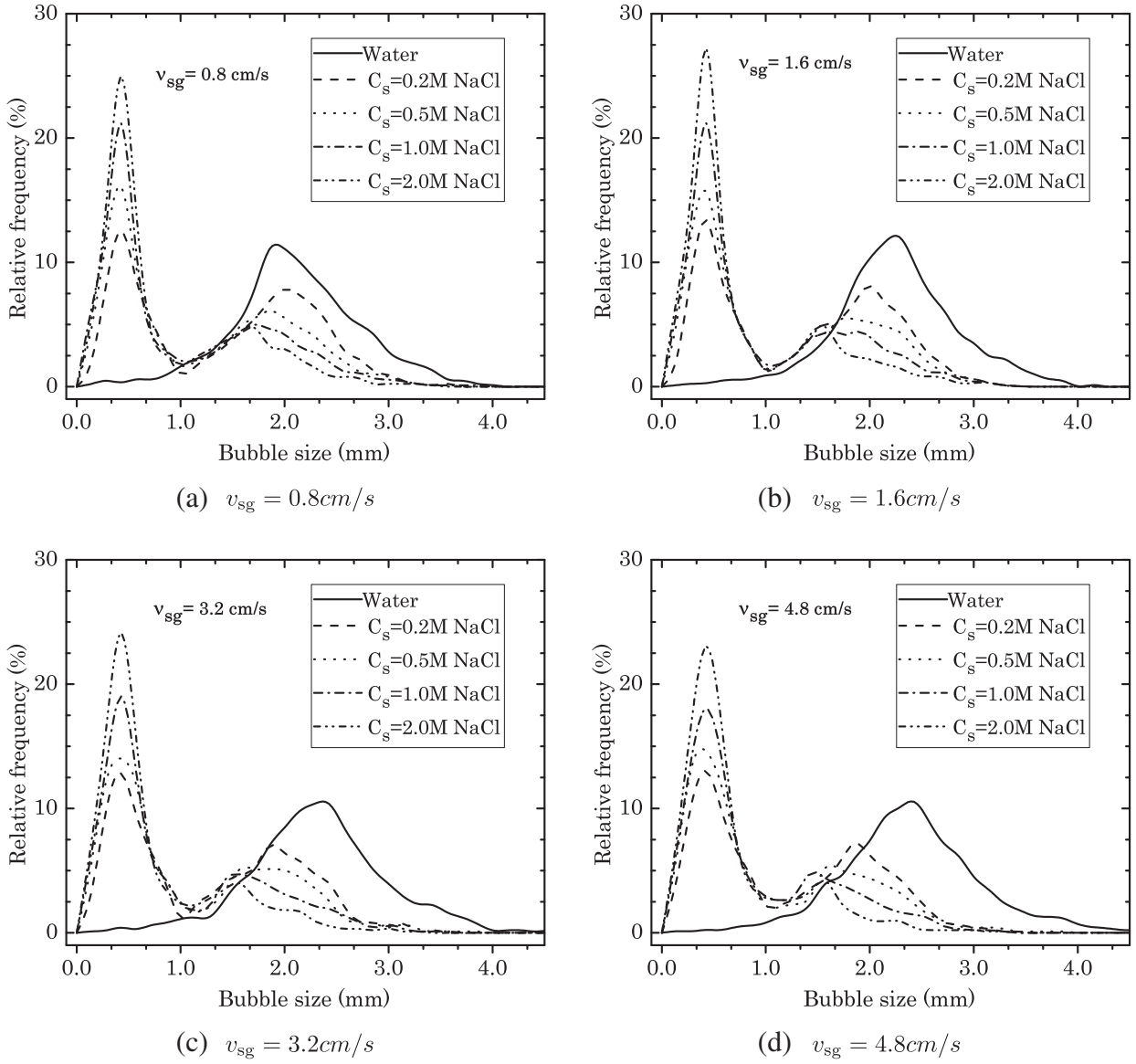

FIGURE 13 Bubble size distribution in the plume above individual sparger for all superficial velocities

Input parameters for the model are the inlet superficial gas velocity, v_{sg}, and average bubble size $d_{b,avg}$, obtained from the BSD at an individual sparger, for the corresponding salt concentration (for example, refer to Figure 5a for v_{sg} = 1.6 cm/s). The model is iteratively solved for gas fractions in the riser (α_R) and downcomer (α_D) sections, and liquid circulation velocity, v_c. Figures 12 and 13 show, respectively, the measured BSD and $d_{b,avg}$, for all salt concentrations (C_s) and superficial velocities (v_{sg}) used in current work.

Increase in gas fractions, due to addition of salt, for riser ($\alpha_{R,salt} - \alpha_{R,nosalt}$) and downcomer sections ($\alpha_{D,salt} - \alpha_{D,nosalt}$), are compared with the average of local gas fractions (from X-ray measurements) in Zones 2 and 4, respectively. Figure 14a,b shows reasonable agreement between the experiments and the 1D model, for different salt concentrations and gas superficial velocities. The global effect of salt is a reduction in the driving force for airlift action (Figure 14c), as a consequence of lower rise velocities of smaller bubbles. This is also reflected through a reduction in liquid circulation velocity v_c, obtained from the model for increasing C_s (Figure 14d). For its simplistic nature and the assumptions, the 1D steady-state drift flux model reasonably explains the effect of salt as primarily through its effect on the average bubble size at the sparger.

8 | DISENGAGEMENT ZONE DYNAMICS

Understanding the interaction of bubbles with the liquid free surface is essential in determining the gas disengagement from the column. For the case of airlift column, free-surface oscillations also have an influence on the gas carryover to the downcomer section. Considering a "degassing" boundary in modeling the top surface introduces a bias in the calculation of the global liquid circulation and can further lead to an underestimation in gas carryover to the downcomer section.[35]

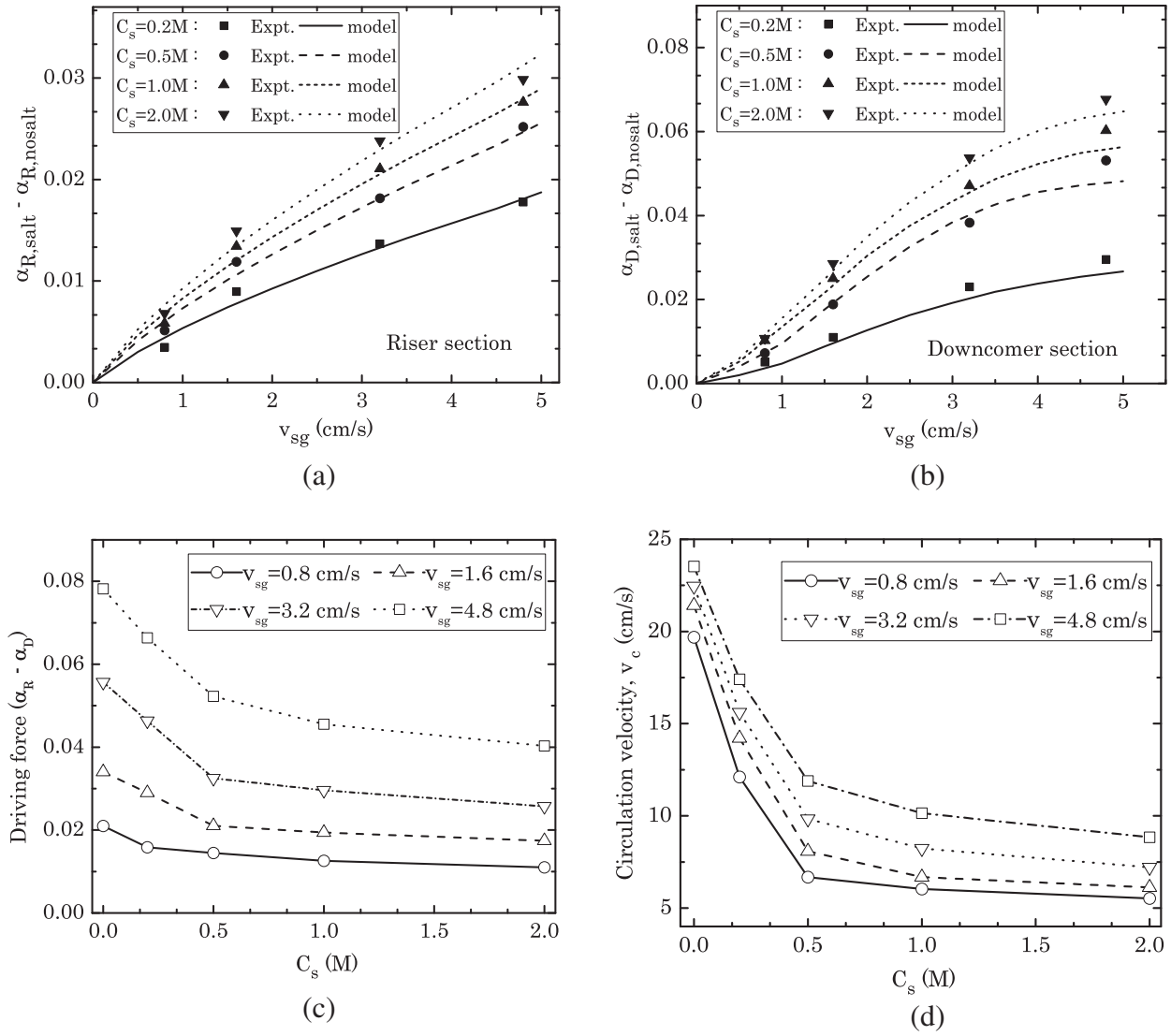

FIGURE 14 (a, b) Comparison of the experimental results with the 1D model: Gas fraction increase due to salt addition in (a) riser section ($\alpha_{R,salt} - \alpha_{R,nosalt}$); (b) downcomer section ($\alpha_{D,salt} - \alpha_{D,nosalt}$). (c) Overall driving force for recirculation $\alpha_R - \alpha_D$ (experimental data from X-ray imaging). (d) Liquid recirculation velocity (from 1D model). The input for the model for various salt concentrations is $d_{b,avg} = f(C_s)$. 1D, one dimensional

In the previous section, behavior of the bubbles at the disengagement zone has been explained using a simple mechanistic model. As seen from the flow profiles (Figure 6), addition of salt leads to formation of a foam layer, which can be attributed to reduction in the bubble sizes and accumulation of these submillimeter size bubbles at the free surface. To better understand the effect of salt and the resultant BSD on the bubble recirculation, a study of the disengagement zone dynamics is necessary. High-speed visualization and BIV techniques are used to this extent.

Figure 15a shows a snapshot and the resultant bubble velocity profile of the disengagement zone for the water case, at v_{sg} = 1.6 cm/s. The free surface forms a spout, with a width stretching till close to mid-downcomer section. A strong upward velocity is maintained in the bubble plume core until the free surface, where the no-shear stress boundary condition changes the flow orientation to horizontal direction. Bubbles to the edge of this plume, are pushed toward the side of the disengagement zone, forming a large vortex above the downcomer section. Close to the wall, the interface is affected by the vortex motion, caused by the recirculation of bubbles (from downcomer section), rising to the surface.

For the salt case (0.2 M NaCl, v_{sg} = 1.6 cm/s), two regions of the foam layer are observed: a stagnant part (above the downcomer section) and a dynamic part (above the riser section), as shown in Figure 15b (left). The dynamic foam layer grows in thickness, due to the accumulation of micron-size bubbles, until sloshed by the kinetic energy dissipation of bubble plumes from the riser section. As the bubbles sizes are much smaller, when compared with the water case, a strong upward flow is not maintained in the core of the bubble plume rising out of riser section (Figure 15b, right). The foam layer acts as a stagnation boundary, making the flow strongly horizontal and thereby steadily

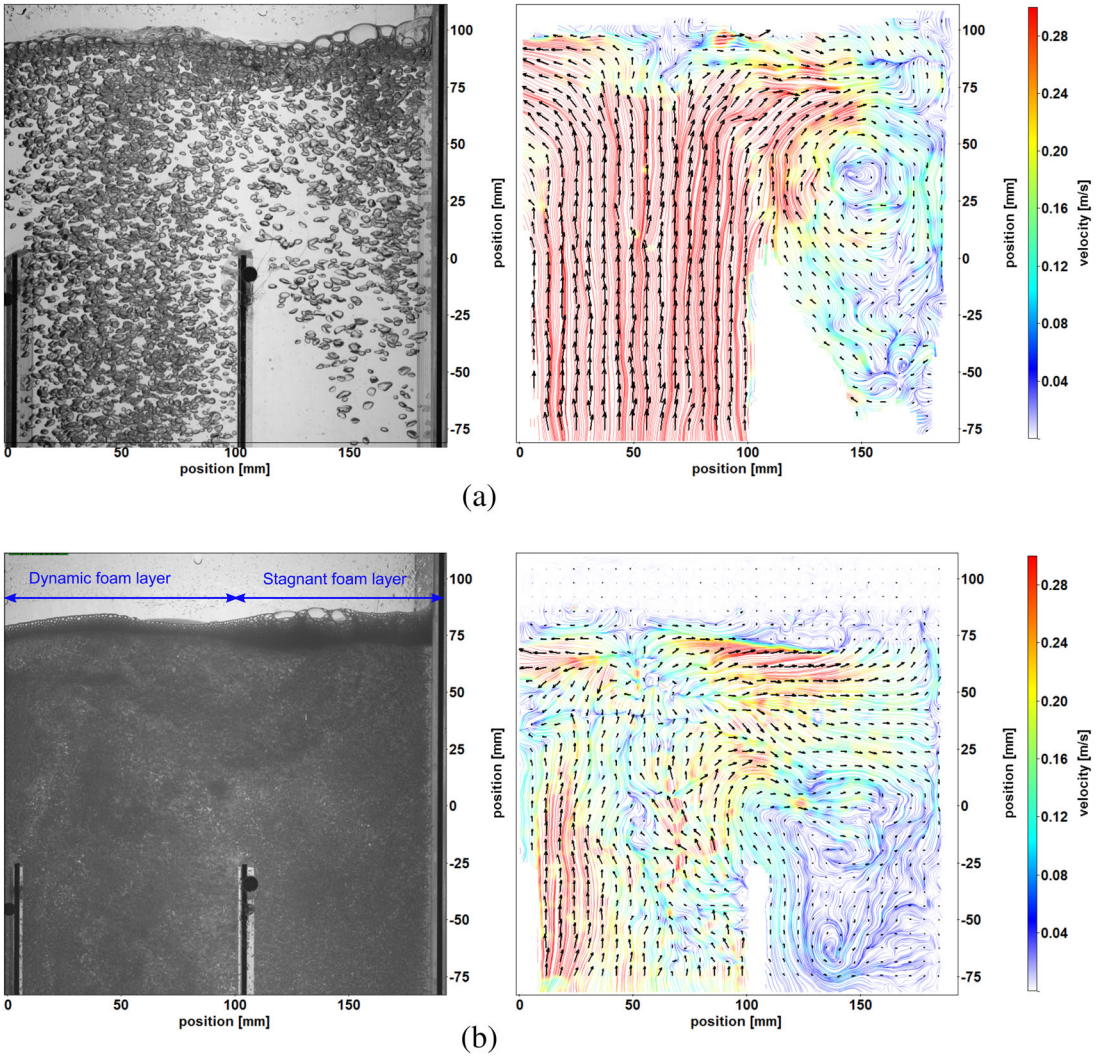

FIGURE 15 Effect of foam dynamics on flow in the disengagement zone: (left) snapshot of the flow pattern and (right) vector arrows and streamline profile from bubble image velocimetry [Color figure can be viewed at wileyonlinelibrary.com]

shearing the dynamic part of the foam layer. These sheared bubbles are dragged toward the column wall and into the downcomer section, leading to additional gas carryover. Unlike the water case, there is no clear vortex in the disengagement zone. Instead, a large meandering low-velocity zone is observed, well into the downcomer.

The role of salt in the dynamics of the disengagement zone is reflected through its effect on the bubble sizes. At higher salt concentrations, a thicker foam layer is observed. The timescale of the foam sloshing depends on the swarm velocity in the bubble clusters, a function of the BSD and the gas superficial velocity. The simple mechanistic model based on the average bubble size, as explained in the previous section, captures the key aspect that larger bubbles from the riser section tend to rise up toward the surface and the smaller ones deviate toward the side of the disengagement zone. Further study of the free-surface foam layer as a boundary condition is essential, as it allows to accurately predict the flow in the downcomer section.

9 | CONCLUSIONS

In the present study, we have performed a detailed experimental investigation into the hydrodynamics of an airlift bubble column, for a wide range of salt concentrations (0–2 M NaCl). Our results explicate that the role of salt is primarily through the coalescence inhibition and resultant impact on the BSD at the sparger. Salt addition creates smaller submillimeter sized bubbles when compared with the pure water case. The BSD at the sparger region dictates the integral bubble plume behavior and the local gas-fraction profiles in the airlift column. A direct consequence of the reduction in bubble sizes is the large residence times of recirculating bubbles and thereby an increase in overall gas fraction, even beyond the transition salt concentration (C_{trans}). The effect of salt through the bubble size can be understood with a simple mechanistic model for the disengagement region.

Salt, through its effect on the bubble size, also leads to formation of a foam layer at the top liquid-free surface, changing the dynamics

of the disengagement region. Qualitative behavior of the disengagement region is studied with a BIV technique. As this region plays an important role in modeling of gas recirculation, understanding the salt effect on bubble sizes can lead to improved models. Further modeling of the free surface should include the foam layer with relevant time scale of foam formation and sloshing. The entire set of data from the current effort can be used to validate more sophisticated models for dense bubbly flows for which does not exist much detailed data; the X-ray imaging proved itself to be a powerful technique to fill this gap.

ACKNOWLEDGEMENTS

This work is part of the Industrial Partnership Programme i36 *Dense Bubbly Flows* that is carried out under an agreement among Nouryon Industrial Chemicals B.V., DSM Innovation Center B.V., SABIC Global Technologies B.V., Shell Global Solutions B.V., Tata Steel Nederland Technology B.V., and the Netherlands Organisation for Scientific Research (NWO). The authors thank Christiaan Schinkel for help with BIV postprocessing and Bert Vreman and Johan Lif for proposing the flow configuration and salt concentration range, for constructive discussions, and for comments on the manuscript. The authors also acknowledge additional financial support from Nouryon PPC business unit.

ORCID

Manas M. Mandalahalli https://orcid.org/0000-0002-3802-3991

REFERENCES

1. Liu W, Moran C, Vink S. A review of the effect of water quality on flotation. *Miner Eng*. 2013;53:91-100.
2. Jean D, Lee D. Effects of salinity on expression dewatering of waste activated sludge. *J Colloid Interface Sci*. 1999;215(2):443-445.
3. Deen N, Mudde R, Kuipers J, Zehner P, Kraume M. Bubble columns. *In: Ullmann's Encyclopedia of Industrial Chemistry*. Weinheim, Germany: Wiley-VCH Verlag GmbH & Co.; 2010:371-375.
4. Heijnen J, Riet KV. Mass transfer, mixing and heat transfer phenomena in low viscosity bubble column reactors. *Chem Eng J*. 1984;28(2): B21-B42.
5. Sharaf S, Zednikova M, Ruzicka MC, Azzopardi BJ. Global and local hydrodynamics of bubble columns–effect of gas distributor. *Chem Eng J*. 2016;288:489-504.
6. Mudde RF, Harteveld WK, van den Akker HEA. Uniform flow in bubble columns. *Ind Eng Chem Res*. 2009;48(1):148-158.
7. Luo HP, Al-Dahhan MH. Local characteristics of hydrodynamics in draft tube airlift bioreactor. *Chem Eng Sci*. 2008;63(11):3057-3068.
8. Quinn J, Maldonado M, Gomez C, Finch J. Experimental study on the shape–velocity relationship of an ellipsoidal bubble in inorganic salt solutions. *Miner Eng*. 2014;55:5-10.
9. Lessard RR, Zieminski SA. Bubble coalescence and gas transfer in aqueous electrolytic solutions. *Ind Eng Chem Fundam*. 1971;10(2): 260-269.
10. Ruzicka M. On dimensionless numbers. *Chem Eng Res Des*. 2008;86 (8):835-868.
11. Craig VS, Ninham BW, Pashley RM. The effect of electrolytes on bubble coalescence in water. *J Phys Chem*. 1993;97(39):10192-10197.
12. Firouzi M, Howes T, Nguyen AV. A quantitative review of the transition salt concentration for inhibiting bubble coalescence. *Adv Colloid Interf Sci*. 2015;222:305-318.
13. Orvalho S, Ruzicka MC, Drahos J. Bubble column with electrolytes: gas holdup and flow regimes. *Ind Eng Chem Res*. 2009;48(17):8237-8243.
14. Besagni G, Inzoli F. The effect of electrolyte concentration on counter-current gas–liquid bubble column fluid dynamics: gas holdup, flow regime transition and bubble size distributions. *Chem Eng Res Des*. 2017;118:170-193.
15. Fu Y, Liu Y. Development of a robust image processing technique for bubbly flow measurement in a narrow rectangular channel. *Int J Multiphase Flow*. 2016;84:217-228.
16. Boyer C, Duquenne AM, Wild G. Measuring techniques in gas–liquid and gas–liquid–solid reactors. *Chem Eng Sci*. 2002;57(16):3185-3215.
17. Gómez-Hernández J, Sánchez-Delgado S, Wagner E, Mudde RF, van Ommen JR. Characterization of tio2 nanoparticles fluidization using x-ray imaging and pressure signals. *Powder Technol*. 2017;316: 446-454.
18. Rabha S, Schubert M, Wagner M, Lucas D, Hampel U. Bubble size and radial gas hold-up distributions in a slurry bubble column using ultrafast electron beam x-ray tomography. *AICHE J*. 2013;59(5): 1709-1722.
19. Kingston TA, Geick TA, Robinson TR, Heindel TJ. Characterizing 3d granular flow structures in a double screw mixer using x-ray particle tracking velocimetry. *Powder Technol*. 2015;278:211-222.
20. Heindel TJ. A review of x-ray flow visualization with applications to multiphase flows. *J Fluids Eng*. 2011;133(7):074001.
21. Kastengren A, Powell CF. Synchrotron x-ray techniques for fluid dynamics. *Exp Fluids*. 2014;55(3):1686.
22. Haynes WM. *CRC handbook of chemistry and physics: a ready-reference book of chemical and physical data*. Boca Raton, FL: CRC Press; 2009.
23. Alles J, Mudde R. Beam hardening: analytical considerations of the effective attenuation coefficient of x-ray tomography. *Med Phys*. 2007;34(7):2882-2889.
24. Ryu Y, Chang KA, Lim HJ. Use of bubble image velocimetry for measurement of plunging wave impinging on structure and associated greenwater. *Meas Sci Technol*. 2005;16(10):1945-1953.
25. Bhakta A, Ruckenstein E. Decay of standing foams: drainage, coalescence and collapse. *Adv Colloid Interf Sci*. 1997;70:1-124.
26. Freire APS, Miranda DD, Luz LM, França GF. Bubble plumes and the coanda effect. *Int J Multiphase Flow*. 2002;28(8):1293-1310.
27. Sánchez Mirón A, Garcia Camacho F, Contreras Gomez A, Grima EM, Chisti Y. Bubble-column and airlift photobioreactors for algal culture. *AICHE J*. 2000;46(9):1872-1887.
28. Kluytmans JH, van Wachem BG, Kuster BF, Schouten JC. Gas holdup in a slurry bubble column: influence of electrolyte and carbon particles. *Ind Eng Chem Res*. 2001;40(23):5326-5333.
29. Ribeiro CP Jr, Mewes D. The influence of electrolytes on gas hold-up and regime transition in bubble columns. *Chem Eng Sci*. 2007;62(17): 4501-4509.
30. Besagni G, Inzoli F. Influence of electrolyte concentration on holdup, flow regime transition and local flow properties in a large scale bubble column. *In: Journal of Physics: Conference Series*. Vol 655. Bristol, UK: IOP Publishing; 2015:012039.
31. Wallis GB. *One dimensional two-phase flow*. New York: McGraw-Hill; 1969.

32. Richardson J, Zaki W. The sedimentation of a suspension of uniform spheres under conditions of viscous flow. *Chem Eng Sci*. 1954;3(2):65-73.
33. Clift R, Grace J, Weber M. *Bubbles, drops and particles*. New York: Academic Press; 1978.
34. Chriastel L, Kawase Y, Znad H. Hydrodynamic modelling of internal loop airlift reactor applying drift-flux model in bubbly flow regime. *Can J Chem Eng*. 2007;85(2):226-232.
35. Talvy S, Cockx A, Line A. Modeling hydrodynamics of gas–liquid airlift reactor. *AICHE J*. 2007;53(2):335-353.

How to cite this article: Mandalahalli MM, Wagner EC, Portela LM, Mudde RF. Electrolyte effects on recirculating dense bubbly flow: An experimental study using X-ray imaging. *AIChE J*. 2019;e16696. https://doi.org/10.1002/aic.16696